Development and Verification of a Laboratory Setup for Testing Space-Based GNSS RFI Monitoring and GNSS-R Analysis Payload and Algorithms

Sahana Bandagadde Umesha, Nikolas Frederik Dütsch, Adonees Semaan, Thomas Pany, *University of the Bundeswehr Munich*

BIOGRAPHY

Sahana Bandagadde Umesha is a research associate at the Institute of Space Technology and Space Applications (ISTA), University of the Bundeswehr Munich, Germany. She holds a B.Tech in Aerospace Engineering from Jain University, India, and a Master's degree in ESPACE from the Technical University of Munich, Germany. Her research interests include GNSS interference analysis, and aiding mechanism for space receivers.

Nikolas Frederik Dütsch is a research associate at the University of the Bundeswehr Munich and works for the satellite navigation unit LRT 9.2 of the Institute of Space Technology and Space Applications. His research focus is on the sensitive detection and geolocation of RF interference sources from LEO satellites. He holds a master's degree in Electrical Engineering from the Friedrich-Alexander-University of Erlangen/Nuremberg, Germany.

Adonees Semaan is currently a research associate and doctoral candidate at the Institute of Space Technology and Space Applications, University of the Bundeswehr Munich. His research focuses on RF engineering for space-based Earth observation, including remote sensing, GNSS-R applications, and radio science.

Thomas Pany is a full professor at Universität der Bundeswehr München at the faculty of aerospace engineering where he teaches satellite navigation. He focuses on GNSS/LTE/5G signal design and processing, software receivers and GNSS/INS/LiDAR fusion. He has about 200 publications including patents and one monography.

ABSTRACT

The reliance on global navigation satellite system (GNSS) has reached a level where interruptions caused by radio frequency (RF) interference, including jamming and spoofing, pose significant societal and economic consequences. Although GNSS has recently demonstrated its potential well beyond Earth, for example, the LuGRE mission (Schauer, 2025). The robustness and reliability of GNSS in terrestrial and near-Earth environments are increasingly challenging. This is further underscored by recent reports of jamming affecting low earth orbit (LEO) satellite constellations, including communication systems such as Starlink (Waterman, 2025). These developments highlight the growing need for space-based radio frequency interference (RFI) monitoring and mitigation capabilities.

Beyond navigation, GNSS signals have also been extensively exploited in remote sensing applications through GNSS reflectometry (GNSS-R), a bistatic radar technique that utilizes reflected GNSS signals to infer geophysical parameters such as surface roughness, ocean state, and wind speed (Martin-Neira, 1993; Komjathy et al., 2000). Both GNSS RFI monitoring and GNSS-R rely on similar payload architectures and signal processing principles, creating opportunities for the development and validation of a shared system.

In this work, we present the development and validation of a configurable software defined radio (SDR) payload for a dedicated small satellite mission called Athene-1, led by the University of the Bundeswehr, Munich, scheduled for launch in 2026 (Bachmann et al., 2024). The payload architecture employs a zenith-facing antenna for direct reception of GNSS signals from medium earth orbit (MEO), and a nadir-facing antenna to capture reflected GNSS signals or emissions from ground-based interference. Both signal streams are subsequently fed to the digital signal processing (DSP) unit, which independently records the time-tagged in- & quadrature-phase (IQ) data at a sampling rate of 20MHz with 4-bit quantization for a duration of 10 minutes. The recorded data is further forwarded to the satellite's data handling subsystem for onboard storage and later downlinked to the ground station.

To ensure robust pre-launch verification, a two-level hardware-in-the-loop testbed has been established, following a staged validation strategy. Stage 1 focuses on laboratory-based end-to-end payload verification using realistic RF signal emulation and geometry replication. Stage 2 foresees the usage of the flight-representative onboard DSP unit within the same hardware chain.

Finally, Stage 3 will address post-launch in-orbit validation using controlled emitter deployments with defined effective isotropic radiated power (EIRP) levels. This staged approach enables systematic assessment and risk reduction, and early identification of error sources and comprehensive validation of both payload architecture as well as associated algorithms prior to launch and in-orbit operations.

Within this framework, the present paper focuses on a representative pseudolite scenario, emulating a spoofing test case. Certain key performance indicator (KPI)s are defined and applied to assess the end-to-end verification strategy, with particular emphasis on signal dynamics, Doppler consistency, and timetag alignment between the zenith and nadir channels. Furthermore, practical limitations and challenges encountered during the laboratory validation are discussed, and representative results are presented to demonstrate the capabilities of the proposed testbed mimicking the payload architecture.

I. INTRODUCTION

The global dependence on GNSS has expanded far beyond the traditional and intended positioning and timing services, becoming a critical component of the transportation, telecommunications, finance, and Earth observation infrastructures. Recent developments have also demonstrated its potential well beyond Earth - for example, the LuGRE mission, which presented the acquisition and tracking of global positioning system (GPS) signals on the lunar surface for the first time ever and achieved a navigation fix - approximately 225,000 miles away from Earth, significantly exceeding the intended range (Schauer, 2025). In parallel, GNSS signals have proven valuable as sources of opportunity for remote sensing through GNSS reflectometry. This bistatic radar technique leverages GNSS signals reflected from the Earth's surface to infer geophysical properties such as ocean roughness, soil moisture, and surface altimetry (Martin-Neira, 1993; Komjathy et al., 2000). GNSS-R's passive nature, global coverage, and all-weather capability have made it increasingly attractive for environmental and climate monitoring missions.

Consequently, GNSS vulnerabilities such as RFI jamming and spoofing events pose increasing risk to both Earthbound and spaceborne applications. Lately, it has also been reported that LEO satellite constellations such as Starlink (and other communication satellites) have also experienced in-space jamming (Waterman, 2025). The availability and reliability of GNSS signals in terrestrial (as well as airborne and spaceborne) environments are increasingly challenged by both intentional and unintentional RFI, and these growing incidents of jamming and spoofing are no longer confined to the research community but have become widely recognized by the general public. Collectively, these findings underscore the growing need for interference monitoring and mitigation strategies.

In light of this, the University of the Bundeswehr, Münich is building its own small satellite mission named Athene-1. The satellite offers a configurable SDR payload that is used for GNSS RFI monitoring and GNSS-R remote sensing applications in addition to other experiments. The satellite substitutes for an experimental laboratory orbiting at an altitude of 505 km, with an inclination of 97.42°, attaining a sun-synchronous orbit in the LEO. With a payload capacity of 75 kg and a takeoff weight of 200 kg, the platform is designed to support a wide range of advanced experiments. These include broadband communications and internet of things (IoT) applications, radio science, GNSS Technologies (occultation, reflectometry, and jamming/spoofing monitoring), optical, and infra-red (IR) Earth Observation, to name a few. For hosting versatile payload modules, the satellite offers a flexible and modular architecture (Bachmann et al., 2024).

The combination of GNSS RFI monitoring and GNSS-R analysis on a common spaceborne platform confers novel capabilities and technical challenges throughout all phases of mission, from pre-launch and in-orbit validation to post-launch operations. Both rely on the sensitive reception/acquisition and processing of weak L-band signals emanating from medium earth orbit ($\sim$22,000 km), often challenged by a dynamic and interference-rich environment. The development and verification of such payload systems supporting these applications necessitate rigorous ground-based testing prior to launch, as post-launch modifications are subject to high constraints. Of equal significance is the development and validation of algorithms for RFI detection, emitter geolocation, and GNSS-R signal retrieval and assessment. In the course of this study, a two-level hardware-in-the-loop testbed has been established to emulate a realistic LEO scenario and conditions. The testbed facilitates end-to-end verification of the payload architecture and yields synthetic, but physically and dynamically consistent datasets for algorithm verification.

This paper addresses the development and verification of such a complex laboratory setup, allowing controlled simulation of GNSS RFI and GNSS-R signals using a dual-channel vector signal generator, integrated with a GNSS SDR and supporting software modules. The proposed paradigm streamlines the systematic testing of signal acquisition, interference detection, and reflectometry algorithms under configurable dynamic scenarios. The observations support the testbed's capability to reproduce a realistic spaceborne signal environment and illustrate its utility as a prelaunch verification platform for space-based GNSS payloads.

II. SYSTEM OVERVIEW

Since the major application-level focus of this paper is in the areas of GNSS RFI monitoring and GNSS-R, it is essential to review the fundamental principles that form the basis of the payload design before delving into the system aspects.

1. GNSS RFI monitoring and reflectometry

Due to the low-power nature of GNSS signals, a weak interference source can cause the receiver to fail or produce hazardously misleading information. Such interferences may originate both from intentional emitters (e.g., jammers, spoofers) or unintentional sources (e.g., space weather or faulty equipment that radiates signals on the L1 frequency). Intentional jamming is designed to overpower the very weak GNSS signals, whereas a spoofing attack attempts to deceive a GNSS receiver by broadcasting incorrect GNSS signals, structured to replicate a set of normal GNSS signals or by rebroadcasting authentic signals captured elsewhere or at a different time (Intertanko, 2019). GNSS RFI monitoring focuses on detecting, characterizing, and geolocating sources of interference that degrade the quality of a GNSS navigation solution.

The relative frequency-of-arrival (FOA) (i.e., the Doppler shift due to the relative motion between the transmitter and receiver) and time difference of arrival (TDOA) of the received signal can be used to estimate the location of the emitter. Previous work, including the one reported by Murrian et al. (2021), has demonstrated the feasibility of space-based RF emitter detection using GNSS payloads deployed on the International Space Station.

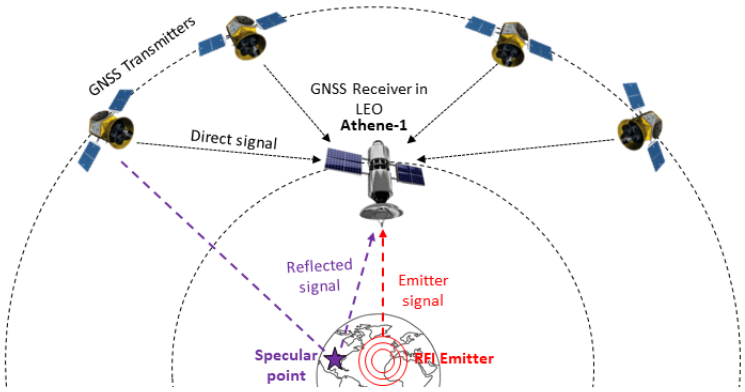


Figure 1: Schematic representation of the combined GNSS-based RFI monitoring and reflectometry concept

In contrast, GNSS reflectometry utilizes the reflected GNSS signal from Earth's surface to infer geophysical properties such as surface roughness, ocean wave height, altimetry, wind speed, and other environmental parameters (Martin-Neira, 1993; Komjathy et al., 2000). Similar to the payload architecture of RFI monitoring, the reflectometry technique relies on a bistatic geometry, where the zenith antenna receives the direct GNSS signals, while the nadir antenna captures the reflected component. By analyzing the Doppler and delay between the two signals, the specular reflection point and scattering characteristics of the surface can be determined.

In space-based RFI monitoring and GNSS reflectometry, the LEO satellite comprises two main functional payloads, that is, the zenith (uplooking) and the nadir (downlooking) antenna. As an element of the navigation subsystem, the zenith antenna includes a space-qualified GPS receiver, which is capable of recording GNSS signals, providing onboard precise navigation solution computation and time information that is in conjunction with a GPS disciplined ultra stable oscillator (USO) for clock generation and time stamping of the received samples. The nadir antenna receives signals from the emitter (or the specular reflection point). The RF front-end (FE) in combination with the DSP unit is responsible for raw signal recording, baseband downconversion, digitization, and sampling of the signals. The specifications and functionalities of the system are detailed in the upcoming section.

2. Payload architecture and the satellite platform

The payload module is designed to perform space-based GNSS signal reception, raw data recording, and on-board processing, while interfacing with the satellite platform for command, control, and telemetry. The architecture, as shown in Figure 2, distinguishes between two RF signal acquisition paths associated with two different antennas: a zenith-pointing GNSS antenna and a nadir-pointing antenna element. This dual antenna configuration enables simultaneous observation and recording of direct GNSS signals from MEO and the interference signals originating from the earth-facing hemisphere, respectively.

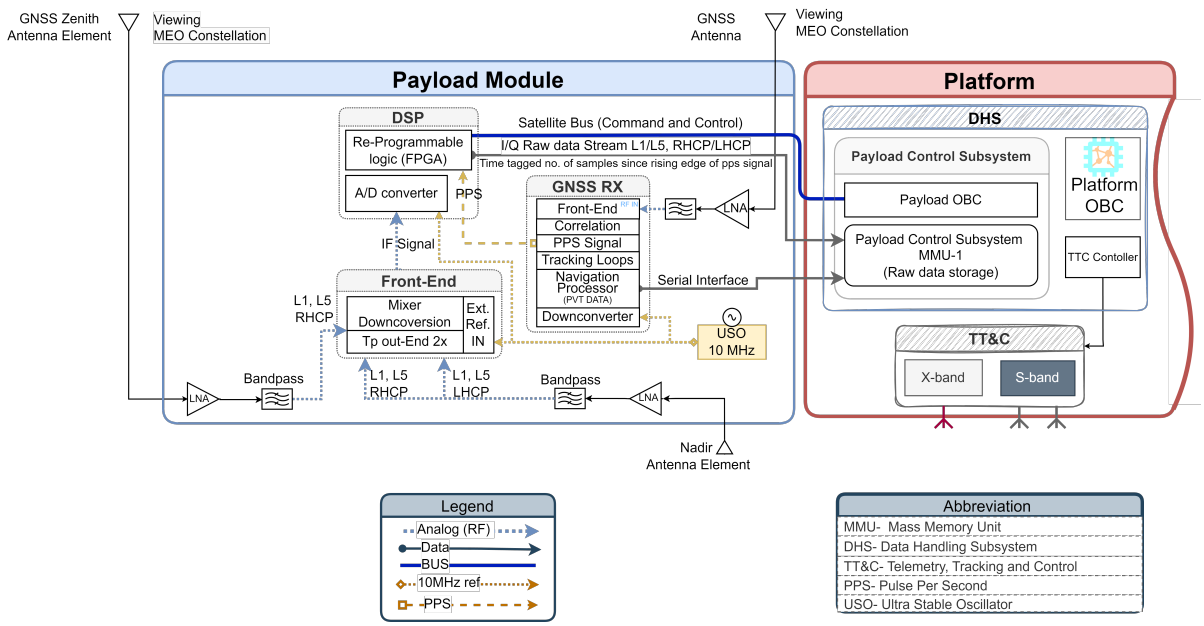


Figure 2: Block diagram of the Athene-1 GNSS payload architecture and its interfaces with the satellite platform subsystems (Image modified based on Duetsch et al. (2022))

In broader aspects, the zenith-pointing antenna supports dual-frequency operation (i.e., L1 and L5), enabling robust reception of GNSS signals. The received RF signals are individually routed through a dedicated bandpass filter and low noise amplifier (LNA) chain to suppress out-of-band interference, minimize noise, and preserve the signal quality. This RF signal is then fed into the GNSS receiver front-end, undergoing signal translation and digitization, representing the nominal GNSS observation chain used for navigation and timing of the spaceborne GNSS signals. Comparably, the nadir-pointing antenna includes the reflected GNSS signals, terrestrial interference, or deliberate emitters such as jammers or spoofers. Similar to the zenith RF chain, the nadir RF path includes a bandpass filter and an LNA to ensure adequate selectivity and sensitivity prior to downconversion. In principle, both Zenith and Nadir signals are fed individually into the same receiver FE and the DSP unit for further processing of signal samples.

The DSP unit on Athene-1 comprises six field programmable gate array (FPGA)-based processing boards (DSP 1-6), with the zenith- and nadir-facing antenna RF output ports connected to DSP-3 and DSP-4, respectively. Each board integrates an Xilinx XCZU15EG FPGA and four AD9371 RF transceivers (NEOSAT GmbH, 2023). The AD9371 contains dual receiver channels, each of which is a direct conversion system that contains a programmable attenuator stage, followed by matched IQ mixers that downconvert received signals to baseband for digitization. The internal analog gain was configured within the range of 0-30dB to ensure optimal utilization of the analog digital conversion (ADC). The receiver includes Σ-Δ ADCs and adjustable sample rates that produce data streams from the received signals. The device's automatic gain control (AGC) loop was enabled and tuned to maintain a constant input level under varying signal conditions, ensuring amplitude stability while maintaining a target root mean square (RMS) voltage level and consistent C/N_0 performance (Analog Devices, 2017).

The DSP platform consists of an internal data storage on board with a capacity of 64 GB, and an 1 Gbit Ethernet interface to provide sufficient bandwidth for uninterrupted streaming of the 20 MHz 4 bit IQ samples to the host.

Both antenna paths converge into a common RF FE and FPGA-based DSP infrastructure, comprising six different FPGA boards. The FE supports an external frequency reference and is disciplined by a 10 MHz ultra stable oscillator, which provides a coherent reference for all local oscillators and sampling clocks, enabling phase-coherent and time-tagged observations. The resulting intermediate frequency (IF) signals from the zenith-facing GNSS antenna and the nadir-facing antenna are digitized by a GNSS SDR platform, which is considered the heart of this system, at a configurable sampling rate and a defined quantization resolution. In nominal GNSS RFI monitoring scenarios, the nadir antenna is assumed to receive only thermal noise in the absence of an interference signal. The raw IQ data streams are transferred via the satellite bus to the data handling subsystem, stored in onboard mass memory, and subsequently downlinked to the ground station for further ground-based post-processing to extract signal processing RFI and GNSS-R observables. An overview of the zenith- and nadir-facing payloads is provided in Figure 3. The recording duration is limited to 10 minutes, consistent with the LEO satellite observation window from the ground station (or emitter), which is approximately 9 minutes and 20 seconds in the considered scenario.

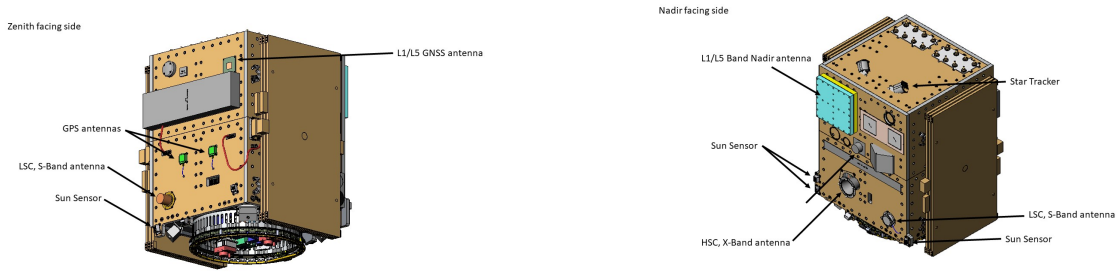


Figure 3: Zenith-facing (left) and nadir-facing (right) of the Athene-1 satellite; Image Credits: LuxSpace (2022)

III. LABORATORY SETUP

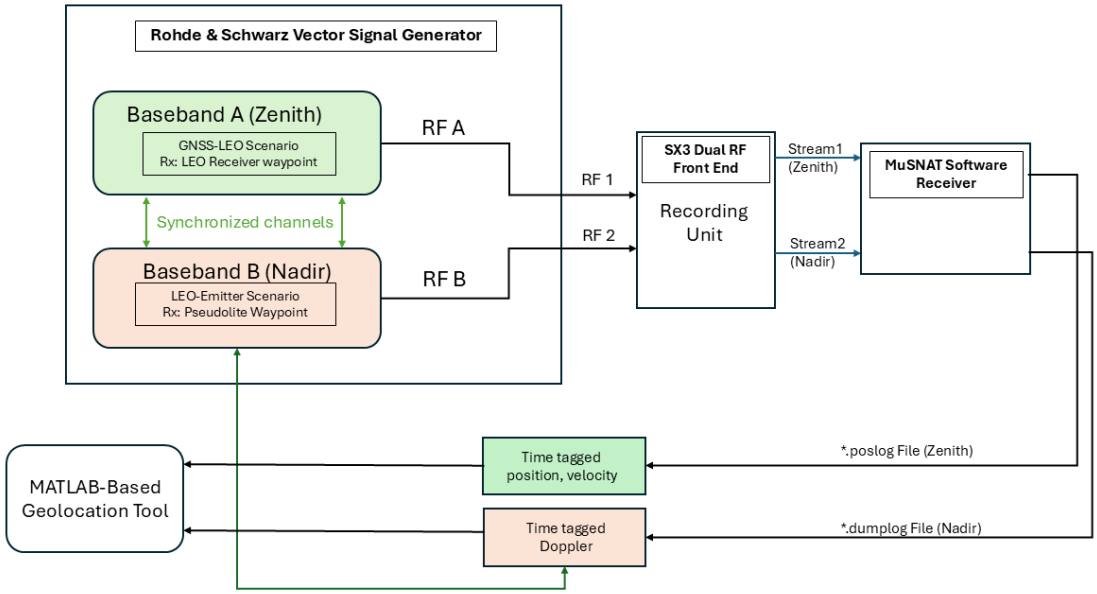


Figure 4: Block diagram of the laboratory testbed for dual-channel GNSS/RFI signal generation, recording, and software-defined receiver processing

Before performing the payload tests with the satellite emulator/Flat-Sat platform, the entire chain is first simulated in a controlled laboratory environment. This very first stage of testing focuses on validating the end-to-end functionality of the components - signal generation, digitization, time synchronization, data storage, and further post-processing of the collected signal samples without involving the actual satellite bus or onboard interfaces. The functional block diagram shown in Figure 4, and the picture of the real setup shown in Figure 5 replicates payload architecture using the Rohde & Schwarz SMW200A Vector Signal Generator, the IFEN SX3 Dual RF Front-End, and software-based post-processing tools such as multi-sensor navigation analysis tool (MuSNAT) (Pany et al., 2019) and MATLAB. In this configuration, the signal simulator generates both the GNSS satellite constellation and the pseudolite signals. In a representative spaceborne scenario, both signals must be generated at the same start time across both the channels uninterruptedly. This is reproduced in the laboratory setup using a common trigger event on the Rohde & Schwarz SMW 200A vector signal generator. Any subsequent trigger event restarts the signals deterministically, providing precise control over timing and repeatability. The time-synchronized RF signals from both basebands are fed into the IFEN SX3 front-end, which performs frequency down-conversion and synchronized digitization between the channels. The FE converts the incoming signals into time-aligned digital intermediate frequency samples with a sampling rate of 20MHz and a 2-bit real IF quantization resolution, and this directly corresponds to the data provided by the onboard DSP in-orbit. This enables detailed testing of the payload's signal behavior and time synchronization under realistic orbital dynamics prior to integration

with the Flat-Sat platform (also called the satellite emulator) in stage 2.

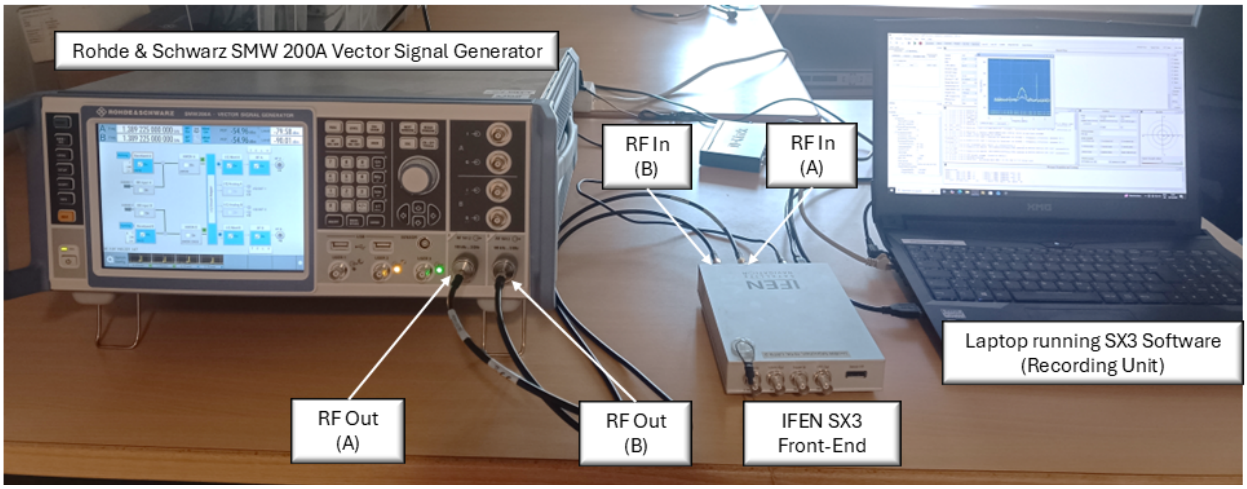


Figure 5: Experimental laboratory setup used for satellite payload testing

Verification strategy for the testbed hardware and software toolchain

A set of KPIs was defined to ensure that the hardware (HW) parts of the testbed, which include the signal generator and the recording unit, as well as the application-specific software (SW) units work as expected. The KPIs are grouped into three main parts to consider different levels of information within the testbed, which are,

- information obtained by processing the nominal GNSS signals of the data link from GNSS MEO constellation to LEO satellite,
- information obtained by processing of ground-based emitted RFI signals or reflected GNSS signals to LEO satellite &
- information obtained from both data channels for RFI monitoring or GNSS-R application purposes.

By processing the nominal GNSS signals with MuSNAT software receiver, which are generated in baseband A (replicating the zenith channel, as shown in Figure 4) of the signal simulator, the position, velocity, and time (PVT) of the LEO satellite, the receiver clock, and clock drift error can be derived. The residual position and velocity errors between the LEO trajectory, which is configured in the signal simulator, and the calculated PVT from MuSNAT, which is derived from the recorded signals of RF channel 1, can be evaluated. The KPIs defined are the bias and standard deviation of the position and velocity residuals. By processing the RFI signal with MuSNAT, which is generated in baseband B (replicating the nadir channel, as shown in Figure 4) of the signal simulator, the frequency shift of the carrier frequency due to the Doppler effect can be measured. The residual error in the frequency shift between the set Doppler, which is configured in the signal simulator, and the measured Doppler of MuSNAT, which is derived from the recorded signal of RF channel 2, can be evaluated. The KPIs are the bias and standard deviation of the Doppler residuals. By combining the PVT information of the LEO satellite from channel A with the correctly time-tagged Doppler measurements of the RFI source from channel B, the emitter can be geolocated. The geolocation error between the set position, which is configured in the signal simulator, and the calculated position can be evaluated. This position error is an additional KPI.

Upon successful validation of this testbed setup, the IFEN SX3 unit can be easily replaced with the actual payload DSP unit of Athene-1, enabling Stage 2 of the validation.

IV. TEST CASE: SPOOFING SCENARIO

This section focuses on the definition and simultaneous simulation of a controlled GNSS, as well as a pseudolite scenario, designed to assess the payload's performance in the presence of a deceptive but structurally valid GNSS signal. For both baseband configurations, the primary objective of the laboratory setup is to clearly replicate the relative geometry and signal dynamics of the MEO-LEO and emitter-LEO, including Doppler evolution, propagation delay, and link duration as mentioned before. Accordingly, the priority was given to the exact reproduction of the geometry over the in-orbit RF environment. To ensure robust acquisition, stable tracking, and clear spectral observability in the laboratory, slightly elevated reference power levels are employed. Since the derived observables vary linearly over signal power, the results can thus be extrapolated to

nominal in-orbit RF conditions.

1. Scenario definition and signal generation

a) Baseband A: Link from GNSS MEO to LEO satellite

Baseband A of the Rohde & Schwarz SMW 200A vector signal generator is configured to generate MEO GNSS signals, as they would have been received by the zenith-facing antenna of the LEO satellite. Therefore, the orbital parameters of a constellation of GPS satellites are loaded into the generator, and for each GPS satellite, an individual pseudo-random noise (PRN) is assigned. The GPS satellite signals are simulated with GPS C/A code only. The trajectory of the LEO satellite is simulated by configuring a moving receiver platform. The receiver trajectory is described by loading a waypoint file of earth centered earth fixed (ECEF) position and velocity vectors with an update rate of 100 Hz. The receiver position states are calculated based on the Keplerian orbit elements of the Athene-1. The main settings for scenario configuration of baseband A are specified in Table 1.

Link budget model:
For a LEO receiver monitored from MEO-GNSS satellite, the received signal power at the LEO receiver can be expressed as,

$$P_{Rx_{GNSS}} = P_{Tx_{GNSS}} - L_{Fs_{GNSS-LEO}} + G_{Rx_{zenith}} \tag{1}$$

where, $P_{Rx_{GNSS}}$ is the received power [dBm], $P_{Tx_{GNSS}}$ is the transmitter output power [dBm], $L_{Fs_{GNSS-LEO}}$ is the free-space path loss (FSPL) [dB], $G_{Rx_{zenith}}$ is the receiver antenna gain = 5dBi. The free-space path loss is computed as,

$$L_{Fs_{MEO-LEO}} = 20log_{10}\left(\frac{4\pi d}{\lambda}\right) \tag{2}$$

where, d is the slant range between the MEO-GNSS satellite and LEO satellite [m], and λ is the wavelength of the signal [m]. With a distance of 21,486 km (GNSS to LEO slant range), a free-space loss of 183dB is obtained. Using Equation 1, with GPS L1 coarse/acquisition (C/A) transmit power of 56.5dBm, FSPL of 183dB and zenith antenna gain of 5dBi in the boresight direction, the resulting received power at the zenith antenna is -121dBm. As indicated in Table 1, the -90dBm received power setting is interpreted as a high-signal-to-noise ratio (SNR) laboratory reference scenario when compared to the nominal in-orbit operations. This configuration was carried out exclusively to observe a clear spectrum and to maintain measurement robustness. The results can be linearly extrapolated to the calculated -121 dBm GNSS reception level in a LEO orbit.

In the overflight geometry, d varies significantly along the pass and is determined from the simulated satellite ephemeris and the assumed emitter coordinates; as a result, $P_{Rx_{GNSS}}$ becomes time-varying.

Table 1: Zenith and nadir antenna channel configurations

Parameter	Zenith (GNSS-LEO)	Nadir (RFI source to LEO)
Date & Time	08-Dec-2025 (13:29:00.000)	08-Dec-2025 (13:29:00.000)
Systems & Signals	GPS L1 (MEO/nominal)	GPS L1 (modified to GEO)
Transmitted frequency	1575.42 MHz	1575.42 MHz
Atmospheric model	None	None
Receiver	Moving (LEO waypoint)	Moving (pseudolite waypoint)
Pseudolite coordinates	n/a	48.1351° N, 11.5820° E
Reference power	-90 dBm	-90 dBm
No. of visible satellites	11	n/a

b) Baseband B: Link from RFI source to LEO satellite

Baseband B of the signal generator is configured to generate RFI emitter signals, as they would be received by the nadir-facing antenna of the LEO satellite. The spatial geometry between the LEO satellite and the emitter source is simulated to determine the link duration and Doppler observables realistically.

Link budget model:
For ground-based emitter monitored from LEO, the received interference power at the satellite antenna can be expressed as,

$$P_{Rx_{RFI}} = P_{Tx_{RFI}} - L_{Fs_{RFI-LEO}} + G_{Rx_{nadir}} \tag{3}$$

where, $P_{Rx_{RFI}}$ is the received power of the RFI emitter signal [dBm], $P_{Tx_{RFI}}$ is the transmitter output power [dBm], $L_{Fs_{RFI-LEO}}$ is the free-space loss [dB], $G_{Rx_{nadir}}$ is the nadir antenna gain = 3 dBi.

Similar to Equation 2, the free-space path loss between the static, ground-based RFI emitter source and the LEO receiver is computed (with a distance of 514 km), resulting in a FSPL of $\sim$ 150dBm. For a transmit power ($P_{Tx_{RFI}}$) of 56.5 dBm with $L_{Fs_{RFI-LEO}}$=150dBm and a nadir antenna gain of 3 dBi, a receiver power ($P_{Rx_{RFI}}$) of -90dBm is attained at the nadir antenna.

To introduce realistic Doppler and propagation delay effects between the LEO satellite and the pseudolite, an external geometry-based modeling approach is employed. Using MATLAB's Satellite Scenario Viewer, the LEO orbit was defined and propagated, which is specified purely based on the Keplerian elements of Athene-1 without the inclusion of perturbations. The pseudolite is modeled analogously to a ground station using fixed geodetic coordinates corresponding to the location of Munich, Germany, as presented in Figure 6.

Based on the resulting relative geometry between the LEO satellite and the pseudolite, Doppler frequency shifts and signal propagation delays are computed over the duration of the visibility window (also referred to as the link time). Subsequently, these observables are converted into a waypoint file that contains position and velocity vectors expressed in ECEF coordinates with a temporal resolution of 100 Hz. A detailed description of the adopted procedure (including limitations to the intrinsic options available within the signal generator) is provided in a subsequent section.

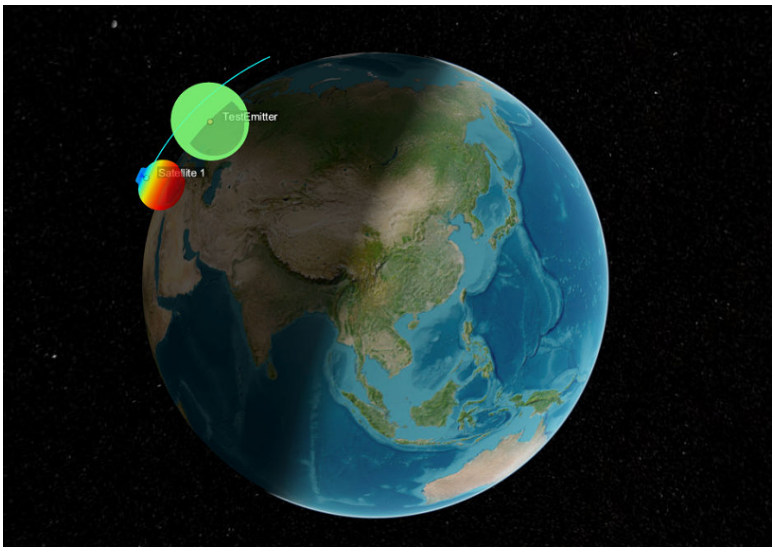


Figure 6: Geometric configuration of the satellite and ground-based emitter for a representative scenario, including the satellite nadir-pointing antenna pattern and the omnidirectional emitter antenna pattern

Figure 7 illustrates the Doppler signature observed by the LEO satellite relative to a ground-based static emitter and its direct relationship to the orbital geometry and line of sight dynamics. In geometrical terms (lower panel of the figure), a static terrestrial emitter radiates a signal toward the nadir-pointing antenna of the Athene-1 satellite, which is relevant for the direct reception of the ground signal. It is worth noting that the observation window (i.e., to be able to establish a link between the ground station and the satellite) of a LEO satellite (in the range of $\sim$500 km) is about 10 minutes from a ground station, which in our case is about 9 min 20 sec, and hence the corresponding Doppler observations are also obtained only for this observation window. During the approaching phase, the projection of satellite velocity onto the emitter-receiver line of sight, i.e., the range rate is negative ($v_r < 0$), yielding a positive Doppler shift ($f_D > 0$). At the point of closest approach, which is at a range of $\sim$508 km in our case, both line of sight (LOS) range rate (v_r) and the corresponding Doppler shift is 0. After passing this point (receding phase), the range rate becomes positive ($v_r > 0$), resulting in a negative Doppler shift ($f_D < 0$). Shortly before and after the zero Doppler phase is the stage with the highest rate of change of Doppler, which in the present study is as large as 550 Hz/s.

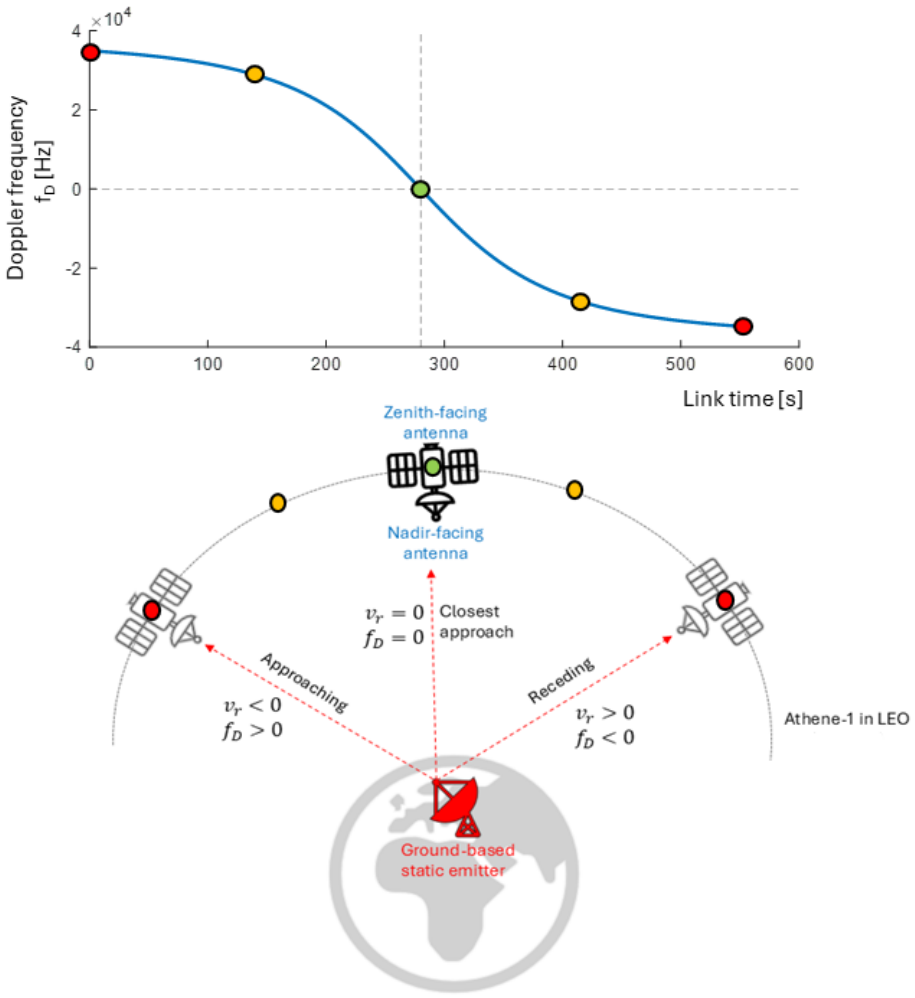


Figure 7: Doppler frequency profile and corresponding LEO satellite-emitter geometry during a single orbital pass

To suppress MEO-induced signal dynamics, a single GPS satellite is configured in baseband B as the spoofing source by modifying its orbital parameters from MEO to geostationary earth orbit (GEO). The resulting GEO-based transmitter, hereafter referred to as a pseudolite, exploits the zero relative Doppler characteristic of geostationary orbits with respect to the Earth. This stationary pseudolite with a stationary signal source corresponding to PRN G01 was fed with an externally generated additional delay and Doppler components in the form of receiver waypoints.

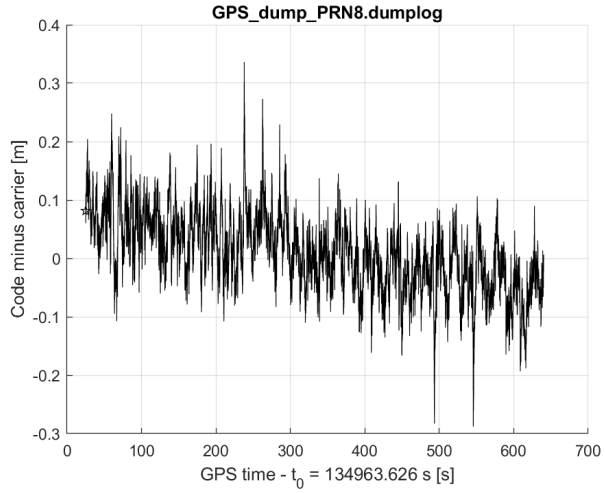
2. Receiver processing results

Upon configuring the signal generation parameters, synchronized signals are generated in both basebands and routed to the IFEN SX3 FE with the RFA output connected to RF1 input of the FE, and the second baseband output (RFB) connected to the corresponding RF input (RF2), as displayed in Figure 5. The FE performs RF filtering, amplification, and downconversion to intermediate frequency. The IF signals are digitized using 2-bit quantization at a sampling rate of 20 MHz and coherently recorded in different signal streams for each channel. No external reference clock is used, and the FE operates on its internal temperature compensated crystal oscillator (TCXO). The recorded IF sample streams are subsequently processed offline by the MuSNAT software receiver.

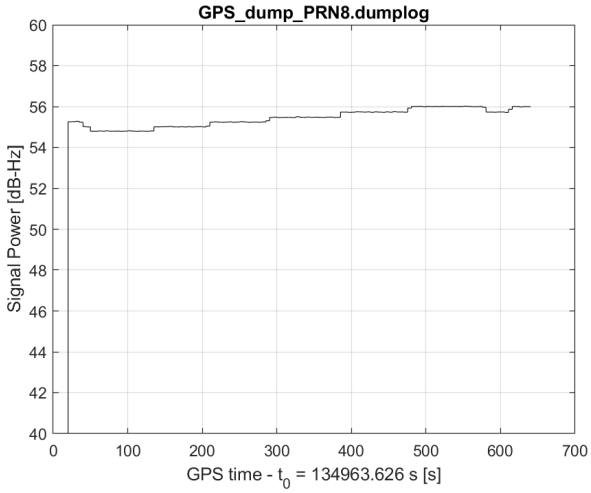
a) Baseband A: Zenith antenna

As the zenith antenna is pointing towards the MEO, all visible GNSS signals were successfully acquired and continuously tracked by the receiver. Code and carrier tracking loops remained locked throughout the observation interval, indicating stable signal conditions and correct FE and sampling configurations. The delay locked loop (DLL), phase locked loop (PLL), and frequency locked loop (FLL) tracking errors remained consistently low throughout the observation window. Such low DLL, PLL, and

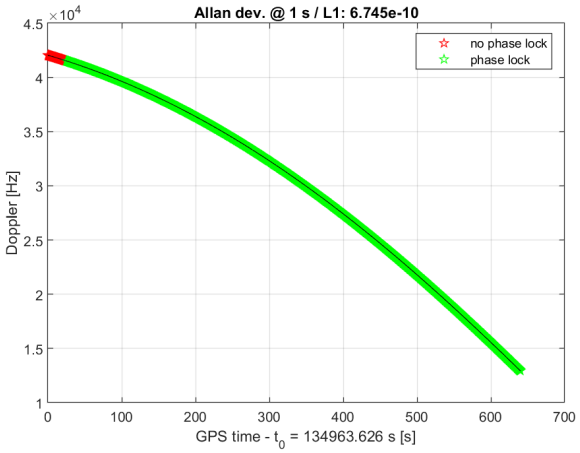
FLL discriminator errors indicated that the code phase alignment with stable pseudorange estimation, precise carrier-phase, and frequency tracking, respectively. No loss of lock (LoL) events, abrupt jitter/divergences were observed for the tracked satellites, confirming robust tracking under the applied signal dynamics, as displayed in Figure 8. The estimated C/N_0 value of $\sim$ 56 dB-Hz remained constant over time and matched the expected levels derived from the laboratory link budget calculations.



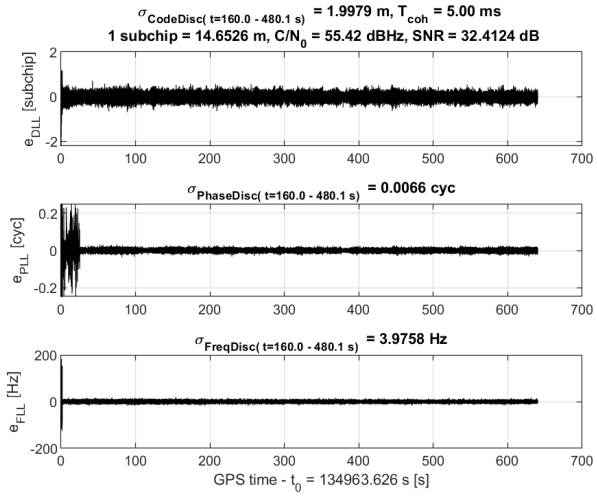
(a) CMC time series - Zenith antenna



(b) Carrier-to-noise density ratio C/N_0 time series - Zenith antenna



(c) Doppler time series - Zenith antenna



(d) Tracking errors - Zenith antenna

Figure 8: Tracking result derived from the zenith antenna RF signal processing

Using these tracked observables from the zenith antenna, MuSNAT was able to compute a continuous and stable PVT solution. The position estimates were consistent with the configured waypoint file, providing a minimal deviation from nominal waypoint values by $\sim$ 0.2m, as portrayed in Figure 9, thus also confirming the defined KPI.

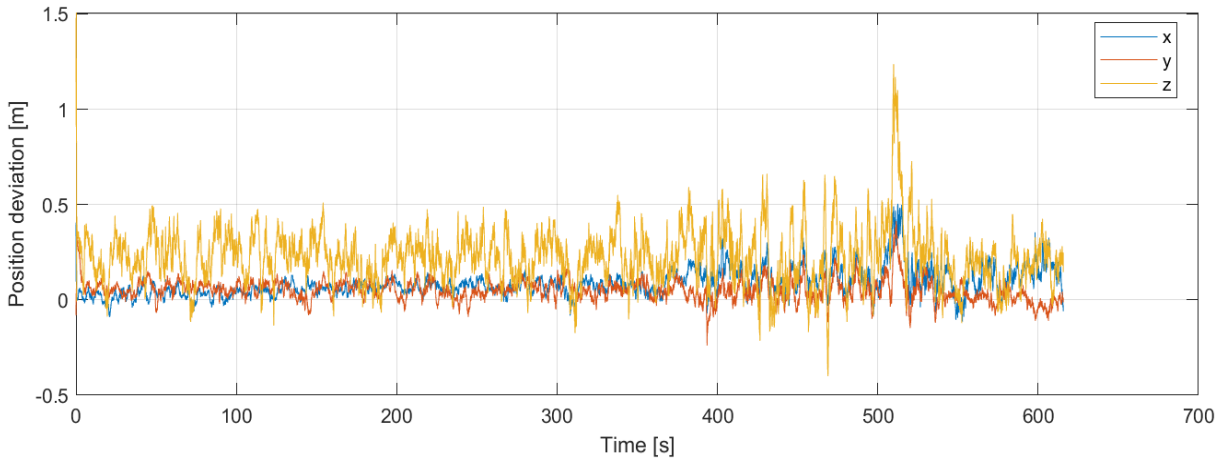


Figure 9: Estimated position accuracy of the LEO satellite trajectory based on zenith RF signals

The receiver clock offset and clock drift were assessed as a part of the PVT solution. As no external clock synchronization was applied between the signal generator and the recording front-end, a non-zero clock offset and clock drift are expected. The estimated clock offset evolved smoothly over time, while the clock drift exhibited a near-quadratic trend, characteristic of an unsynchronized local oscillator, with a mean value of -1.234 $\mu s/s$. This behavior of the clock drift is further smoothed based on a quadratic fitting as seen in Figure 10, which serves as a critical reference for analyzing the results from the nadir channel described in the upcoming section.

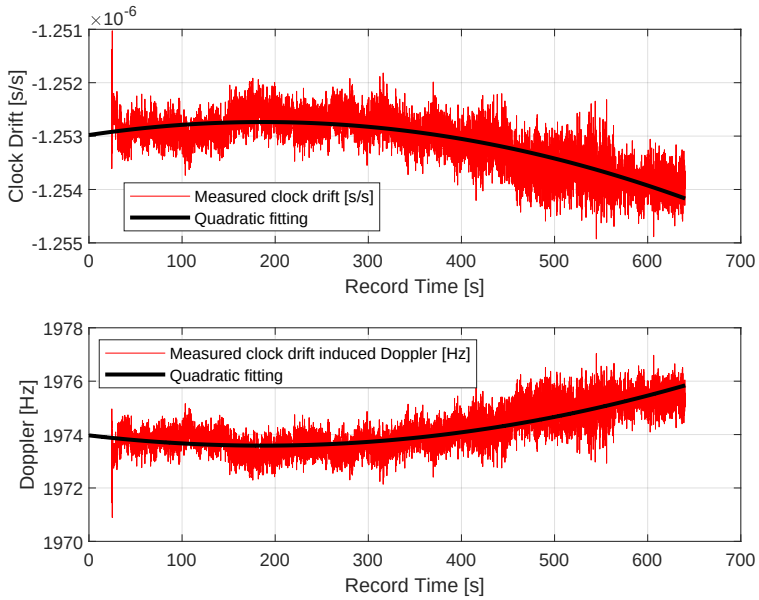


Figure 10: Clock drift estimation over time and its induced Doppler effect. The upper panel shows the measured clock drift (red) with a quadratic fit (black), and the lower panel shows the corresponding Doppler shift induced by clock drift, along with its quadratic trend.

b) Baseband B: Nadir antenna

The nadir-pointing antenna channel was used to track the pseudolite signal transmitting the GPS G01 PRN code. The RFI signal was successfully acquired and continuously tracked by MuSNAT software receiver despite significantly higher dynamics associated with the relative motion between the RFI source and the satellite. Stable tracking loop operation was maintained throughout the processing interval/observation window, indicating reliable code phase alignment, carrier-phase tracking and frequency estimation, with no loss of lock events or abrupt jumps, including the direct overhead region where the Doppler rate

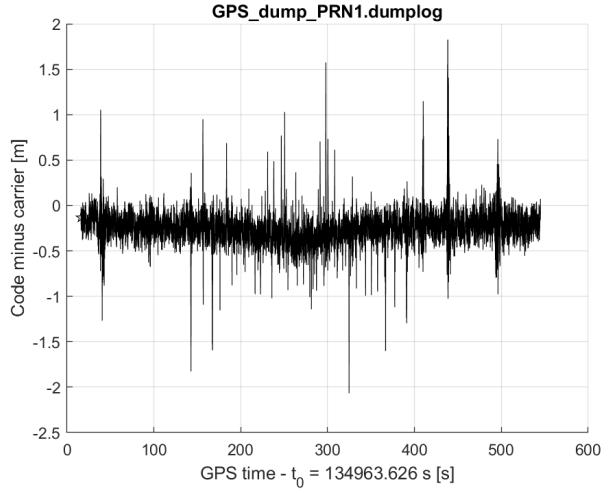
reached values up to 550 Hz/s. These results validate that the pseudolite signal characteristics were fully compatible with the receiver tracking architecture.

The estimated Doppler frequency (between the LEO satellite as a receiver and the emitter) exhibited a deterministic behavior dominated by two components. The first component corresponds to the configured relative motion between the pseudolite signal source and the receiver, as defined in the signal generator. The second component is an additional Doppler term induced by the receiver clock drift. Given that the zenith and nadir signals are sampled with the same clock signal, the calculated/derived clock drift from the zenith signal is the same for the nadir signal. The clock drift estimated from the zenith antenna PVT solution is therefore used as a reference to quantify the clock-induced Doppler component of the nadir signal. This presents as a nearly quadratic frequency bias superimposed on the nominal Doppler profile, with a consistent magnitude and sign. Mathematically, this can be expressed as,

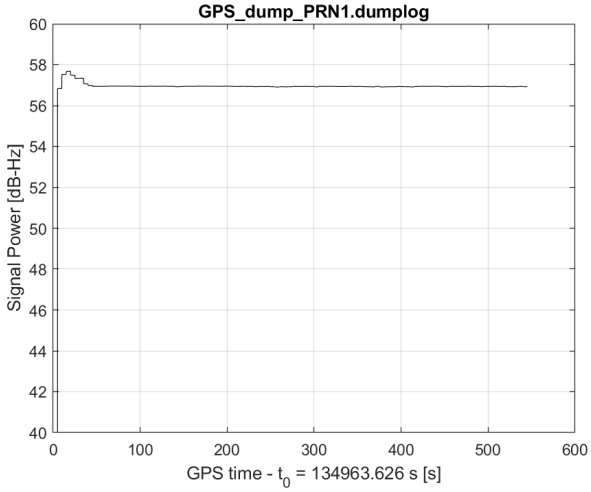
$$f_D(t) = f_{geometry}(t) + f_{clock}(t), \tag{4}$$

$$f_{clock}(t) = -f_c \delta\dot{t}_r(t), \tag{5}$$

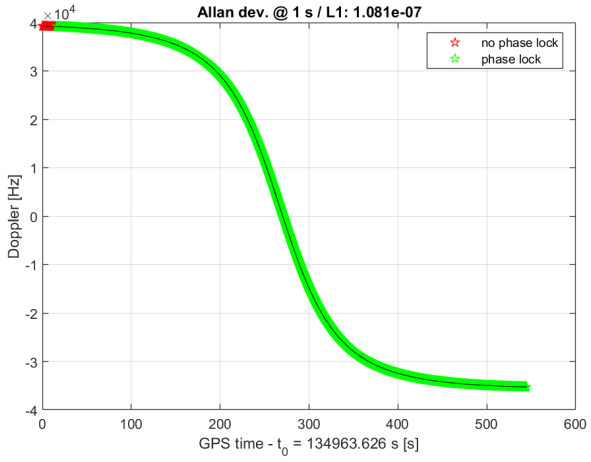
where f_c denotes the carrier frequency (i.e., 1575.42 MHz) and $\delta\dot{t}_r$ is the receiver clock drift.



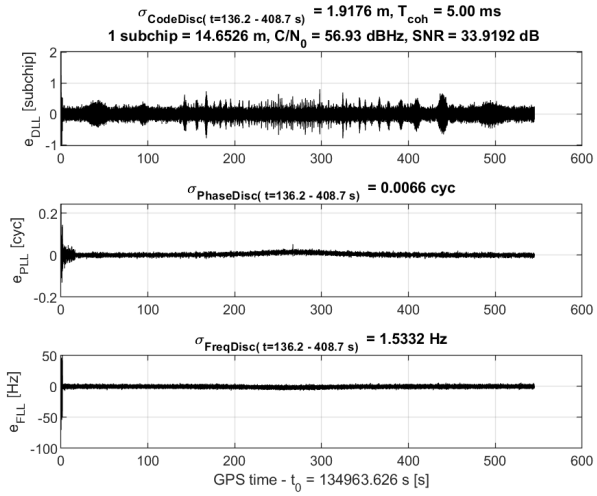
(a) CMC time series - Nadir Antenna



(b) Carrier-to-noise density ratio C/N_0 time series - Nadir Antenna



(c) Doppler time series - Nadir Antenna



(d) Tracking errors - Nadir Antenna

Figure 11: Tracking results derived from the nadir antenna RF signal processing

c) Doppler residuals analysis

Once the tracking results from the pseudolite signal are obtained, it is meaningful to assess whether the laboratory testbed (including the software receiver) operates reliably under the defined scenario conditions and does not introduce any unintended or systematic artifacts into the measurement chain. Doppler measurements from the tracked RFI signal provide a particular sensitive indicator of such a behavior as they directly reflect both the imposed geometry based signal dynamics as well as the tracking performance. Moreover, in addition to precise PVT information, Doppler observables form a central input to the final stage of the experiment, namely the geolocation of the ground-based RFI emitter. Accordingly, the Doppler domain is selected as the primary validation metric, and a detailed comparison is performed between the Doppler profile fed to the signal generator and the Doppler measured at the receiver.

In order to correctly assess the residual Doppler error between the set Doppler profile in the signal generator and the measured Doppler, some important processing steps must be conducted in advance. Since the signal generation process begins before starting the actual RF sample recording, the time of the first measured Doppler value is delayed to the first Doppler, which is configured in the signal simulator. The measured Doppler values must be time-tagged with the absolute GNSS time of the scenario. Therefore, on the one hand side, the two channels of the signal simulator have to be precisely time-synchronized to each other, and on the other hand side, the start of recording of both channels must be at the same time. If the testbed fulfills both conditions, then the clock error in both sample streams is the same. The clock error can be determined by processing the GNSS signals from the zenith channel. The relative time of Doppler measurements, which are natively time-stamped according to the elapsed sample time since the start time of the first recorded sample, can now be linked to the absolute GNSS time. Before the residuals between the set Doppler of the scenario and measured Doppler of the RFI source can be calculated, the measured Doppler values have to be corrected by the clock drift induced Doppler of the recording clock.

Upon having the fed Doppler, measured Doppler and the clock-drift induced Doppler on the same timescale, the Doppler measurements can be compared and the corresponding Doppler residuals can be compared as follows:

$$Residuals = f_{D_{measured}} - \left(f_{D_{fed}} + f_{D_{clock-drift}}\right) \tag{6}$$

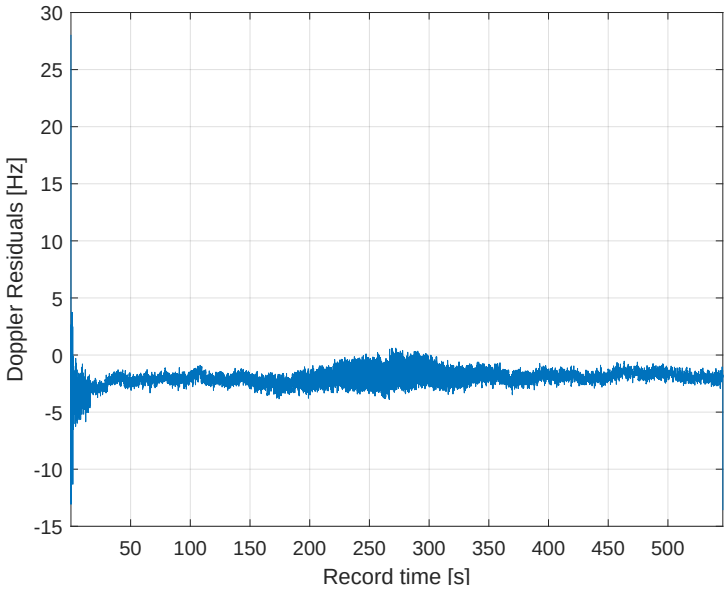


Figure 12: Doppler residuals

As illustrated in Figure 12, the residual Doppler error has a nearly constant bias of -2 Hz and a standard deviation of $\sim$ 0.62 Hz. The exact cause of this constant bias is under further investigation. At the scenario time of 200 to 300s, the maximum change in Doppler occurs, which leads to slightly higher Doppler residuals. Notwithstanding, the absence of systematic bias or long-term divergence in the Doppler residuals provides a strong end-to-end validation of the laboratory setup, spanning signal generation, front-end recording, receiver tracking, clock drift estimation, and time alignment. Overall, this demonstrates that the dominant Doppler components are accurately modeled and no unintended systematic frequency distortions are introduced within the scenario by the laboratory setup.

3. Emitter geolocation

The geolocation of the emitter is determined by using the GPS time-tagged Doppler information from the RFI signal and the PVT information of the satellite. The FOA measurement is related to the unknown emitter position according to

$$f_{oA} = \frac{1}{\lambda_0}\left(-\frac{v_{Sx}\ (x_S - \hat{x}_E) + v_{Sy}\,(y_S - \hat{y}_E) + v_{Sz}\,(z_S - \hat{z}_E)}{\sqrt{(x_S - \hat{x}_E)^2 + (y_S - \hat{y}_E)^2 + (z_S - \hat{z}_E)^2}} + c_0\left(\delta\hat{\dot{t}}_E - \delta\dot{t}_R\right)\right) \tag{7}$$

in which $\hat{x}_E$, $\hat{y}_E$ and $\hat{z}_E$ are the unknown ECEF position coordinates of the RFI source, $\delta\hat{\dot{t}}_E$ is the unknown clock drift of the emitter, v_{Sx}, v_{Sy} and v_{Sz} are the known satellite velocity components, x_s, y_s and z_s are the known satellite position coordinates, λ_0 is the carrier-wavelength at the center frequency of L1, c_0 is the light speed, and $\delta\dot{t}_R$ is the measured receiver clock drift error (Teunissen and Montenbruck, 2017). The four unknowns can be estimated by using at least four FOA measurements. During one satellite overflight normally more than four FOA measurements are available, which leads to an overdetermined equation system. The nonlinear set of equation systems must be solved iteratively. Starting from an initial guess of the emitter position and performing a first-order linearization of the equations around the starting point, the least squares solution of the estimated states is found. In general, several iterations are necessary until the least squares solution converges (Yaakov et al., 2002).

Upon convergence of the iterative least-squares process, the estimated state vector is obtained as,

$$\hat{x} = [\hat{x}_E \quad \hat{y}_E \quad \hat{z}_E \quad \delta\hat{\dot{t}}_E]. \tag{8}$$

The estimated emitter position is evaluated against the known reference coordinates used for the scenario definition and signal generation. The geolocation error vector is defined as,

$$e = \hat{x}_E - x_E. \tag{9}$$

Based on this, the horizontal and vertical error components are obtained by transforming the ECEF error vector into the geodetic coordinate system.

For the considered scenario, the defined as well as the geolocated emitter coordinates are presented in Table 2. The geolocated position is $\sim$ 5km deviated from the set coordinates of the emitter position. Within the current scenario, it is presumed that a slight temporal offset ($\sim$ 0.1s) between the receiver position and the corresponding Doppler values exists, which directly impacts the combined geolocation accuracy. Upon correction, the algorithm is expected to converge better and provide more accurate geolocation of the emitter.

Table 2: Geolocated coordinates of the pseudolite

Parameter	Defined coordinates	Geolocated coordinates
Latitude	48.0810 [deg]	48.1076 [deg]
Longitude	11.6276 [deg]	11.6233 [deg]
Altitude	540 [m]	507 [m]

V. LIMITATIONS AND PRACTICAL CONSIDERATIONS

1. High dynamics emulation constraints

Several practical challenges were encountered during the payload validation campaign, primarily driven by the pronounced relative dynamics between the LEO satellite and the ground-based RFI emitter, as well as by intrinsic limitations of the employed signal generator. Based on the considered geometry, the expected Doppler rate can reach values of up to approximately 550 Hz/s (at the closest approach), thereby imposing stringent requirements on the realism of the signal dynamics emulation.

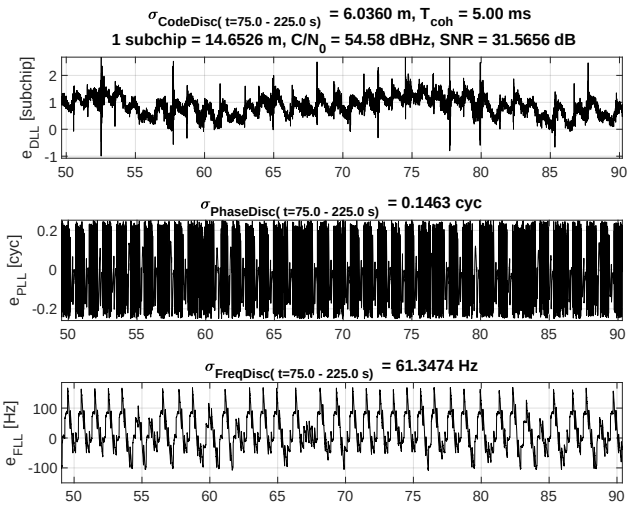


Figure 13: Unstable tracking behavior of the pseudolite based on the intrinsic pseudorange error profile of the signal generator

During the initial laboratory setup, the pseudolite behavior was emulated using the signal generator's built-in pseudorange error injection functionality. This approach relied on externally defined scenario-specific pseudorange error profiles to impose the desired relative motion effects. However, post-processing of the recorded samples revealed significant instability in the receiver tracking loops, characterized by abrupt frequency deviations of approximately 50 Hz in the measured FLL tracking errors as seen in Figure 13. This behavior was primarily attributed to limitations in the signal generator's internal handling of the pseudorange error profile. In particular, update interval of 100 ms constrains the temporal resolution of the applied dynamics, forcing the signal generator to perform linear interpolation between successive points. For scenarios with high Doppler rates, this is insufficient to accurately reproduce the rapid frequency variations, resulting in the unstable/degraded tracking performance.

As a consequence, the use of the signal generator's inherent pseudorange error injection was deemed unsuitable for high-dynamic test cases of this nature. At the time of testing, no alternative native functionality was available within the employed signal generator to support continuous, high-rate Doppler evolution with adequate temporal resolution. This limitation constitutes a key constraint of the current laboratory setup and motivated the adoption of alternative signal generation strategies for subsequent experiments.

2. Hardware-software combined challenges

In a setup that combines several hardware and software components, additional challenges and error sources naturally arise. These include RF impairments from the hardware, as well as clock offsets and drift between independently operating units. Together, these effects influence key observables (such as the C/N_0, Doppler, PVT) and can reduce the robustness of the software receiver tracking loops, especially under high-dynamic conditions. As a result, these limitations must be considered when interpreting the experimental results.

3. Practical workarounds

A possible solution to circumvent these limitations in the signal generation process of highly dynamic scenarios is described in the following paragraph. The main idea is to simulate the LOS dynamics of the nadir link as it was a GNSS-like scenario, omitting the application of additional pseudo-range offsets on the PRN signal itself. This is done by re-configuring the orbital parameters of satellite PRN G01 to a geostationary orbit. The geostationary satellite acts as the RFI source. The key is to find a moving receiver trajectory containing the same pseudo-range and range-rate profiles as they were obtained from a LEO satellite to earth-bounded emitter geometry. In Figure 14 on the left side, the receiver trajectory and the static position of satellite PRN G01 are depicted. The geostationary satellite is set in the equatorial plane, therefore the z-component of the ECEF position vector is equal to zero. The current receiver position, which is indicated by the blue dot, moves in the xy-plane from the top to the bottom of the Figure. The update rate of the receiver waypoints is set to 100 Hz. This high update rate is a key advantage of this approach and the main reason for its use, as such fine temporal resolution was not possible with the intrinsic pseudorange profile options of the signal generator.
In the first phase, it approaches the geostationary satellite as far as the closest distance between receiver and satellite is reached, and in the second phase, the receiver moves away from the satellite. On the right side, the corresponding Doppler profile in

dependence on the simulation time is visualized. As the receiver moves with a nearly constant velocity of around 7.69 km/sec, the LOS range-rate is negative in the first phase, which leads to the positive Doppler, and vice-versa for the second phase.

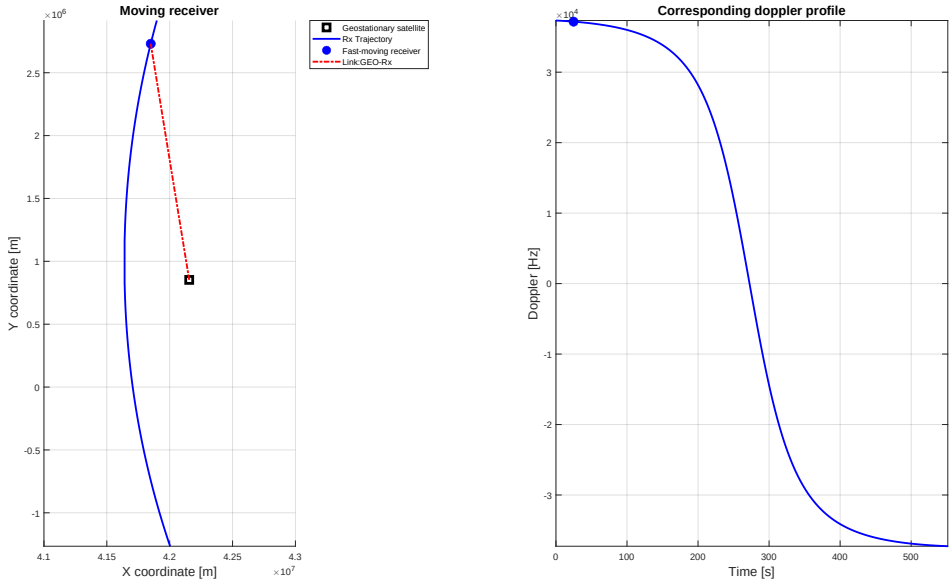


Figure 14: Visualization of the moving receiver trajectory (solid blue line) with respect to geostationary satellite (black square). The distance between the current receiver position (blue dot) and the geostationary satellite is indicated by the red dashed line (left Figure) with corresponding Doppler profile over scenario time (solid blue line) (right Figure). The blue dot indicates the current Doppler values at the position of the moving receiver.

The generation of the waypoint file based on the scenario Doppler profile and the set position of the geostationary satellite is described in the following procedure:

1. *Inputs*
   (a) Read the Doppler profile from the RFI scenario.
   (b) Read the range at closest approach between LEO satellite and emitter for the overflight.
   (c) Specify the velocity of the moving receiver. (Receiver movement with constant velocity assumed)
   (d) Specify the x, y, z ECEF coordinates of the geostationary satellite.
2. *Trajectory start position definition*
   (a) Determine the unit vector between the origin of the coordinate system and the geostationary satellite and multiply it by the minimum range. This vector is the displacement vector from the position of the geostationary satellite towards the receiver position, which is defined in the xy-plane.
   (b) Calculate the position vector of the receiver start position by subtracting the displacement vector from the geostationary position vector.
3. *Velocity vector at start position*
   (a) Determine the orientation of the unit velocity vector at start by applying either a 90° clockwise or counter-clockwise rotation on the unit position vector in the xy-plane. The rotation in a clockwise direction is for the lower part of the receiver trajectory towards the negative y-direction, and the opposite rotation is for the upper part of the trajectory towards the positive y-direction.
   (b) Determine for each direction the start velocity vectors by multiplying the unit velocity vector by the input velocity.
4. *Receiver waypoint profile generation (for upper and lower part of the trajectory)*

(a) Determine the next waypoint by updating the position vector with a position vector increment. This increment is calculated based on the fixed geometric distance between subsequent waypoints and the orientation of the velocity vector in the xy-plane.

(b) Determine the updated LOS velocity vector between the updated position vector and the geostationary satellite.

(c) Read in the next Doppler value based on the scenario and determine the magnitude of the LOS velocity component.

(d) Create an updated receiver velocity vector based on the velocity vector with the update in the LOS velocity direction.

(e) Repeat steps (a) to (d) until the end of Doppler values is reached.

5. *Merge upper and lower trajectory part for the combined receiver trajectory*

VI. CONCLUSION AND OUTLOOK

This study demonstrates the feasibility of Doppler-based emitter geolocation using GPS time-tagged RFI measurements and satellite PVT information within a controlled laboratory environment. The observed consistency between injected and receiver-estimated Doppler confirms the integrity of the signal generation, recording, receiver tracking, and processing chain, supporting the validity of the derived geolocation results.

Future work will extend the laboratory setup in three ways. First, on the signal side, the scope will be expanded beyond a controlled pseudolite configuration to encompass more complex spoofing scenarios including multi-spoofers with relative time offsets, jamming with different waveforms such as continuous wave, chirp, and GNSS reflectometry to emulate specular point evolution and validate delay-Doppler models.

Second, from a timing perspective, different oscillator error models will be systematically evaluated, and their impact on Doppler observables, time-tag alignment between the zenith and nadir RF channels, and geolocation accuracy will be quantified with particular emphasis on USO error representations based on Allan Deviation, including random walk and drift components.

Finally, the verification roadmap will progress beyond the current laboratory configuration toward flight-representative validation. Stage 2 (pre-launch payload tests) will replace the IFEN SX3 FE with the Athene-1 onboard DSP unit and verify end-to-end equivalence in sample timing, quantization, AGC/FE behavior, and the data throughput on a continuous basis for the defined record duration without any loss of samples/packets. Stage 3 (post-launch) will address in-orbit validation through dedicated measurement campaigns, including controlled emitter antenna selection, EIRP and location for safety and compliance during a chosen overflight. The staged approach enables systematic testing and validation of both the payload and associated algorithms in a controlled laboratory environment, serving as a reference for subsequent verification stages and allowing potential error sources to be identified and mitigated prior to in-orbit deployment.

ACKNOWLEDGEMENT

This research paper in the project SeRANIS is funded by dtec.bw – Digitalization and Technology Research Center of the Bundeswehr. dtec.bw is funded by the European Union - NextGenerationEU.

REFERENCES

Analog Devices (2017). Integrated, Dual RF Transceiver with Observation Path-AD9371. Datasheet Revision B, Analog Devices, One Analog Way, Wilmington, MA. `https://www.analog.com/`.

Bachmann, J., Kinzel, A., Porcelli, F., Schmidt, A., Schwarz, R., Hofmann, C., Förstner, R., and Knopp, A. (2024). SeRANIS: In-Orbit-Demonstration von Spitzentechnologie auf einem Kleinsatelliten. *Deutscher Luft- und Raumfahrtkongress 2022, Dresden*, page 12 pages. Artwork Size: 12 pages Medium: application/pdf Deutsche Gesellschaft für Luft- und Raumfahrt - Lilienthal-Oberth e.V. Version Number: 1.0.

Duetsch, N., Jaiswal, R., Ernest, H., Foerstner, R., and Pany, T. (2022). Design and Development of a Dedicated LEO Satellite Payload for Detection and Localization of Earth-Bounded GNSS Interference Sources for the Seamless Radio Access Network for Internet of Space (SeRANIS) satellite mission. In *Proceedings of the 73rd International Astronautical Congress (IAC 2022)*, Paris, France. International Astronautical Federation (IAF).

Intertanko (2019). Jamming and Spoofing of Global Navigation Satellite Systems (GNSS). Technical report, Maritime Global Security, Intertanko.

Komjathy, A., Zavorotny, V. U., Axelrad, P., Born, G. H., and Garrison, J. L. (2000). Gps signal scattering from sea surface: Wind speed retrieval using experimental data and theoretical model. *Remote Sensing of Environment*, 73(2):162–174.

LuxSpace (2022). OHB-Tochterunternehmen LuxSpace und die Universität der Bundeswehr München unterzeichnen Vertrag für SeRANIS-Mission auf Basis von Triton-X-Plattform. https://luxspace.lu/.

Martin-Neira, M. (1993). A passive reflectometry and interferometry system (paris): Application to ocean altimetry. *ESA Journal*, 17:331–355.

Murrian, M. J., Narula, L., Iannucci, P. A., Budzien, S., O'Hanlon, B. W., Psiaki, M. L., and Humphreys, T. E. (2021). First results from three years of GNSS interference monitoring from low Earth orbit. *NAVIGATION*, 68(4):673–685.

NEOSAT GmbH (2023). Payload Design Description. Technical Report 1.1, NEOSAT GmbH. https://www.neosat.de/.

Pany, T., Dötterböck, D., Gomez-Martinez, H., Hammed, M. S., Hörkner, F., Kraus, T., Maier, D., Sanchez-Morales, D., Schütz, A., Klima, P., and Ebert, D. (2019). The Multi-Sensor Navigation Analysis Tool (MuSNAT) – Architecture, LiDAR, GPU/CPU GNSS Signal Processing. In *Proceedings of the 32nd International Technical Meeting of the Satellite Division of The Institute of Navigation (ION GNSS+ 2019)*, pages 4087–4115.

Schauer, K. (2025). NASA Successfully Acquires GPS Signals on Moon. Technical report, NASA Goddard Space Flight Center.

Teunissen, P. J. and Montenbruck, O., editors (2017). *Springer Handbook of Global Navigation Satellite Systems*. Springer International Publishing, Cham.

Waterman, S. (2025). GPS Jamming Extends to Low-Earth Orbit as Pentagon Races to Bolster Constellation. *Air & Space Forces Magazine*.

Yaakov, B.-S., X. Rong, L., and Thiagalingam, K. (2002). Linear Estimation in Static Systems. In *Estimation with Applications to Tracking and Navigation*, pages 121–177. John Wiley & Sons, Ltd. Section: 3 _eprint: https://onlinelibrary.wiley.com/doi/pdf/10.1002/0471221279.ch3.